Prediction of an U_2S_3-type polymorph of Al_2O_3 at 3.7 Mbar

Koichiro Umemoto* and Renata M. Wentzcovitch

Minnesota Supercomputing Institute and Department of Chemical Engineering and Materials Science, University of Minnesota, 421 Washington Avenue SE, Minneapolis, MN 55455

We predict by first principles a phase transition in alumina at ≈3.7 Mbar and room temperature from the $CaIrO_3$-type polymorph to another with the U_2S_3-type structure. Because alumina is used as window material in shock-wave experiments, this transformation should be important for the analysis of shock data in this pressure range. Comparison of our results on all high-pressure phases of alumina with shock data suggests the presence of two phase transitions in shock experiments: the corundum to $Rh_2O_3(II)$-type structure and the $Rh_2O_3(II)$-type to $CaIrO_3$-type structure. The transformation to the U_2S_3-type polymorph is in the pressure range reached in the mantle of recently discovered terrestrial exoplanets and suggests that the multi-megabar crystal chemistry of planet-forming minerals might be related to that of the rare-earth sulfides.

alumina | first-principles calculation | high-pressure phase transition | postperovskite | rare-earth sulfide structure

Alumina, Al_2O_3, is an important compound in high-pressure technology and geophysics. It is used as window material in shock-wave experiments (1). Ruby, Al_2O_3 doped with chromium, serves as a pressure calibrant in diamond-anvil-cell experiments (2). In the Earth's mantle, Al_2O_3 is a major chemical component in solid solution with $MgSiO_3$ garnet, perovskite (PV), and postperovskite (PPV). This formation of solid solutions with alumina changes the properties of the pure phases, such as their equations of state, thermoelastic properties, phase boundaries, electrical conductivity, oxidation, and spin states of iron impurities in $MgSiO_3$, etc. (e.g., refs. 3–9).

The experimental and theoretical literature on phase transitions in Al_2O_3 is quite extensive (10–19). Two pressure-induced transitions have been predicted theoretically (10–12, 16–18) and confirmed experimentally (13–15, 19): from corundum (space group $R\bar{3}c$), the stable ambient form, to the $Rh_2O_3(II)$-type structure (space group $Pbcn$) at ≈80–100 GPa and then to the $CaIrO_3$-type PPV structure (space group $Cmcm$) at ≈130 GPa. These pressures are realized in the Earth's mantle. The $CaIrO_3$-type polymorph is the highest-pressure form identified experimentally so far for both Al_2O_3 and $MgSiO_3$. A phase transition in the $CaIrO_3$-type phase in Al_2O_3 or $MgSiO_3$ should change the properties of their solid solution, a key input in the modeling of planetary interiors. A first-principles study predicted the dissociation of $CaIrO_3$-type $MgSiO_3$ into CsCl-type MgO and cotunnite-type SiO_2 at ≈1.1 TPa (20), a pressure relevant for the giant planets and exoplanets. The same type of dissociation was also predicted for $NaMgF_3$, a low-pressure analog of $MgSiO_3$ (21). However, $CaIrO_3$-type Al_2O_3 is expected to undergo a nondissociative *post*-PPV transition because the equivalent dissociation products (AlO and AlO_2) are unlikely to form. Here, we report the first-principles prediction of a phase transition in Al_2O_3 from the $CaIrO_3$-type polymorph to another with the U_2S_3-type structure. The latter structure was suggested as a potential post-PPV structure in ABX_3 compounds in the absence of a dissociation transformation; in $MgSiO_3$ and $NaMgF_3$, the U_2S_3-type phase remains metastable with respect to their dissociation products (22).

Computational Details. Calculations were performed by using the local-density (LDA) (23) and generalized-gradient approximations (GGA) (24). The valence electronic configurations used for the generation of Vanderbilt ultrasoft pseudopotentials (25) are $3s^23p^03d^0$ and $2s^22p^4$ for Al and O, respectively. Their cutoff radii are 1.8, 1.8, and 2.0 a.u. for Al and 1.0 and 1.0 a.u for O. The plane-wave cutoff energy is 150 Ry. We used variable-cell-shape molecular dynamics (26, 27) for structural optimization under arbitrary pressures. Dynamical matrices were computed at wave vectors **q** by using density-functional perturbation theory (28, 29). The numbers of formula units in the unit cells, **k** points in the irreducible wedge, and **q** points are (2, 10, 4) for corundum, (4, 4, 8) for $Rh_2O_3(II)$-type, (2, 24, 6) for $CaIrO_3$-type, and (4, 3, 8) for U_2S_3-type Al_2O_3. Force constants are extracted to build dynamical matrices at arbitrary phonon **q** vectors. Vibrational contributions to the free energy are calculated by the quasi-harmonic approximation (QHA) (30). In this approximation, the free energy is

$$F(V, T) = E_0(V) + \frac{1}{2} \sum_{i,\mathbf{q}} \hbar \omega_{i,\mathbf{q}}(V)$$
$$+ \sum_{i,\mathbf{q}} k_B T \log\left(1 - \exp\left(-\frac{\hbar \omega_{i,\mathbf{q}}(V)}{k_B T} \right) \right), \quad [1]$$

where $E_0(V)$ is the static total energy and $\omega_{i,\mathbf{q}}(V)$ are the phonon frequencies. The numbers of **q** points in the irreducible Brillouin zone used for the summation in Eq. **1** are 116, 196, 124, and 112 for corundum, $Rh_2O_3(II)$-type, $CaIrO_3$-type, and U_2S_3-type Al_2O_3 respectively. Calculations were done using the Quantum-ESPRESSO package (31).

Results and Discussion

The U_2S_3-type structure (Fig. 1) is closely related to the $CaIrO_3$-type structure (32). The space group of the U_2S_3-type phase is $Pmcn$ (or $Pnma$ in the standard setting), which is a subgroup of $Cmcm$, $CaIrO_3$-type phase's space group. During the transformation the octahedral layers of the latter connect and produce the U_2S_3-type structure with a continuous 3D network of Al–O bonds.

The calculated equations of states shown in Table 1 are consistent with those of previous studies (16–18). Static enthalpy calculations (Fig. 2) clearly show the sequence of stable phases. The static transition pressures using the LDA (GGA) are 82 (88), 137 (145), and 373 (380) GPa for corundum-to-$Rh_2O_3(II)$-type,
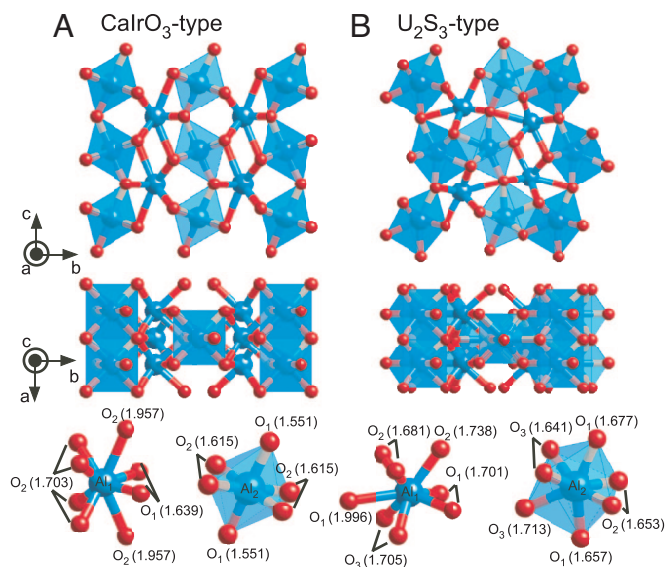
Fig. 1. Crystal structures of CaIrO$_3$-type (*A*) and U$_2$S$_3$-type Al$_2$O$_3$ (*B*). Blue and red spheres denote aluminum and oxygen, respectively. Al$_1$ and Al$_2$ are aluminum in the A and B sites, respectively. Polyhedra are drawn only around Al$_2$ for visualization purposes. For the CaIrO$_3$-type phase at 400 GPa, lattice constants are (*a*, *b*, *c*) = (2.264, 7.332, 5.658) Å. Atomic coordinates are Al$_1$ (4*c*) (0, 0.2516, 0.75), Al$_2$ (4*a*) (0, 0, 0), O$_1$ (4*c*) (0, 0.9134, 0.75), and O$_2$ (8*f*) (0, 0.3525, 0.4298). For the U$_2$S$_3$-type phase at 400 GPa, lattice constants are (*a*, *b*, *c*) = (2.287, 6.350, 6.359) Å. Atomic coordinates are Al$_1$ (4*c*) (0, 0.2535, 0.8051), Al$_2$ (4*c*) (0, −0.0597, −0.0143), O$_1$ (4*c*) (0, 0.9494, 0.7254), O$_2$ (4*c*) (0, 0.3752, 0.0500), and O$_3$ (4*c*) (0, 0.3092, 0.3835), in the *Pmcn* setting where the inversion center is set at (1/4, 1/4, 0) for comparison with the CaIrO$_3$-type phase. In the standard *Pnma* setting, lattice constants and atomic coordinates of the U$_2$S$_3$-type phase are (*a*, *b*, *c*) = (6.359, 2.287, 6.350) Å, Al$_1$ (4*c*) (0.8051, 0.25, 0.5035), Al$_2$ (4*c*) (−0.0143, 0.25, 0.1903), O$_1$ (4*c*) (0.7254, 0.25, 0.1994), O$_2$ (4*c*) (0.0500, 0.25, 0.6252), and O$_3$ (4*c*) (0.3835, 0.25, 0.5592). Numbers in parentheses represent Al–O bond lengths in angstroms at 400 GPa.

Rh$_2$O$_3$(II)-type-to-CaIrO$_3$-type, and CaIrO$_3$-type-to-U$_2$S$_3$-type transitions, respectively. These pressures are consistent with results from other calculations (16–18). A transition to the *P6$_3$/mmc* structure, another candidate form for a post-PPV phase found in NaMgF$_3$ (22), was not found in Al$_2$O$_3$ up to 700 GPa. In NaMgF$_3$ the U$_2$S$_3$-type phase is produced by a soft phonon in the CaIrO$_3$-type phase. In Al$_2$O$_3$ no phonon softening is observed in the CaIrO$_3$-type and in the U$_2$S$_3$-type phases at least up to 700 GPa (Fig. 3). Therefore, both phases should be dynamically stable within this pressure range. Comparison between the crystal structures of the two polymorphs shows that the average Al$_1$–O and Al$_2$–O bond lengths (see Fig. 1, legend) decrease and increase across the phase transition, respectively, producing more similar aluminum polyhedra with coordination 8(= 7 + 1) and 7 as opposed to 8(= 6 + 2) and 6 as in the CaIrO$_3$-type phase. This change is illustrated in Fig. 1, where the average Al$_1$–O bond length is shown to change from 1.751 Å to 1.739 Å, whereas the Al$_2$–O bond length changes from 1.594 Å to 1.662 Å at 400 GPa. These changes produce an elongation in the crystal structure along the *a* and *c* axes and a compression along *b*; *b* and *c* become very close to each other and the U$_2$S$_3$-type phase becomes slightly less anisotropic than the CaIrO$_3$-type phase. U$_2$S$_3$-type Al$_2$O$_3$ remains insulating. The LDA electronic band gaps of the U$_2$S$_3$-type phase are 6.7 and 6.4 eV at 400 and 700 GPa, respectively. When the U$_2$S$_3$-type phase is decompressed, it transforms back to the CaIrO$_3$-type phase below 150 GPa.

The quasi-harmonic phase boundaries in the Al$_2$O$_3$ system are displayed in Fig. 4. The corundum-to-Rh$_2$O$_3$(II)-type and

Table 1. The third-order Birch–Murnaghan equation of states for Al$_2$O$_3$ polymorphs calculated by LDA

Phase	Source	V, a.u.^{3}	B, GPa	B'
Corundum				
0 GPa, static	Present calc.	283.46	259.8	4.02
	Calc. (16)	273.30	248	4.13
	Calc. (17)	286.32	252.6	4.237
0 GPa, 300 K	Present calc.	286.73	251.0	4.04
	Calc. (18)	286.23	240.5	3.94
	Exp. (33)	287.81	254.4	4.275
Rh$_2$O$_3$(II)-type				
0 GPa, static	Present calc.	276.88	264.7	3.93
	Calc. (16)	267.57	252	4.07
	Calc. (17)	279.53	258.2	4.140
80 GPa, 300 K	Present calc.	227.62	544.8	3.37
	Calc. (18)	225.94	530.2	3.33
CaIrO$_3$-type				
0 GPa, static	Present calc.	269.42	251.6	4.11
	Calc. (16)	261.70	231	4.38
	Calc. (17)	271.90	241.6	4.464
	Exp. (19) (300 K)	267.23	249	4 (fixed)
150 GPa, 300 K	Present calc.	198.38	786.8	3.24
	Calc. (18)	196.68	762.6	3.31
U$_2$S$_3$-type				
400 GPa, static	Present calc.	155.83	1,562	3.01
400 GPa, 300 K	Present calc.	156.56	1,552	3.00

Rh$_2$O$_3$(II)-type-to-CaIrO$_3$-type phase boundaries have negative Claperyron slopes (17, 18), $dP/dT = \Delta S/\Delta V$. In contrast, the CaIrO$_3$-type–U$_2S_3$-type phase boundary has a positive slope of + 9.3 MPa/K at 1,000 K. This positive slope can be understood on the basis of the vibrational density of states (VDOS). Fig. 5 shows that peaks at low frequencies shift upward across the post-PPV transition, reflecting the shorter average Al$_1$–O distances in the U$_2$S$_3$-type phase. This decreases the vibrational entropy change across the transitions and the relative stability of
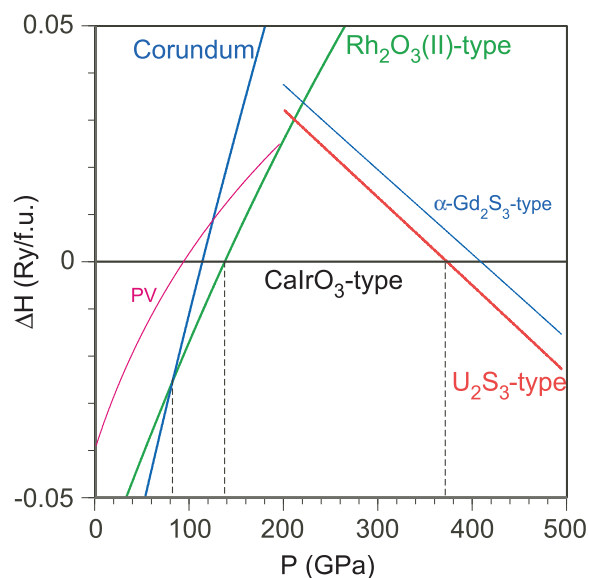

Fig. 2. Relative static LDA enthalpies of Al$_2$O$_3$ polymorphs with respect to the CaIrO$_3$-type phase. Dashed vertical lines denote corundum-Rh$_2$O$_3$(II)-type, Rh$_2$O$_3$(II)-type to CaIrO$_3$-type, and CaIrO$_3$-type to U$_2$S$_3$-type transition pressures, respectively. The perovskite form of Al$_2$O$_3$ does not have a stability field, consistent with previous calculations (16–18).
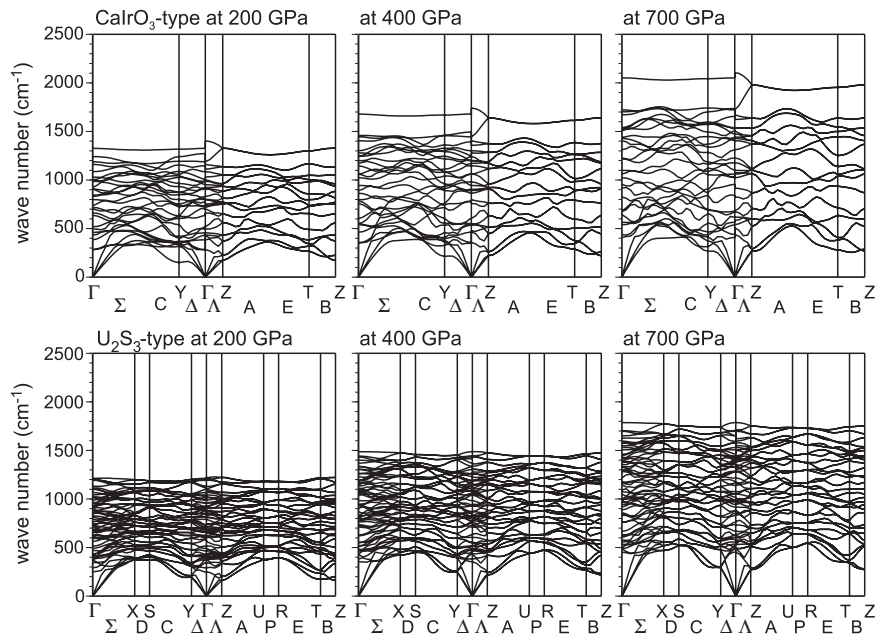
Fig. 3. Phonon dispersions of CaIrO$_3$-type and U$_2$S$_3$-type Al$_2$O$_3$ show no instabilities up to 700 GPa. Pressures are static LDA values.

the U$_2$S$_3$-type phase with increasing temperature. The downward shift of the high-frequency peak reflects the increase of the average Al$_2$–O distances, increasing the entropy. The influence of the low-frequency modes is predominant in the entropy and
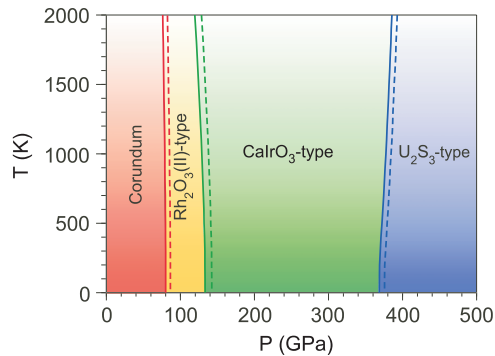

Fig. 4. Calculated phase boundaries in Al$_2$O$_3$. Solid (dashed) lines denote the LDA (GGA) results. The CaIrO$_3$-type to U$_2$S$_3$-type transition pressures by LDA (GGA) are 369 (376) GPa at 0 K, 370 (377) GPa at 300 K, 378 (385) GPa at 1,000 K, and 386 (393) GPa at 2,000 K.
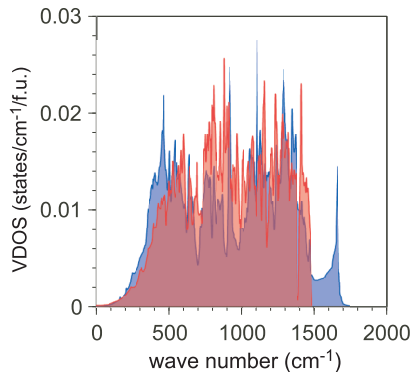

Fig. 5. Phonon densities of states of CaIrO$_3$-type (blue) and U$_2$S$_3$-type (red) Al$_2$O$_3$ at 400 GPa.

the Clapeyron slope remains positive even at high temperatures. However, this downward frequency shift at high frequencies produces a peculiar phase boundary with positive slope but slightly negative curvature; the Clapeyron slopes at 1,500 K and 2,000 K are +8.2 and +7.7 MPa/K, respectively.

Al$_2$O$_3$ is important for dynamic compression technology, because it is used as window material. In raw shock data to 340 GPa, no direct evidence of phase transition was noticed, although there was an atypical relationship between shock velocity (u_s) and particle velocity (u_p): $u_s = C + S u_p$ in which S (0.957) is unusually small, implying a possibility of sluggish phase transformations (34). However, a comparison between our static LDA results on Al$_2$O$_3$ and raw shock data to 340 GPa (34, 35) strongly suggests the presence of all three phases stable below 340 GPa in the shock data (Fig. 6). With shock data alone, it is difficult to resolve phase transitions accompanied by small density changes that could be comparable to the limit of detectability. The transition pressures in shock data are much higher than the calculated ones. This suggests that the phase transitions in Al$_2$O$_3$ have considerable hysteresis. This is consistent with observations from static compression experiments in which sample annealing was necessary for phase transitions (15, 17, 19). According to Fig. 6, the transition pressure from the corundum to Rh$_2$O$_3$(II)-type phase in shock experiments should be ≈120 GPa. It is interesting to note that this transition pressure is close to the pressure at which optical transparency (36) and electrical resistivity (37) were reduced in shock compression, implying a strong relationship between these reductions and the corundum-to-Rh$_2$O$_3$(II)-type phase transition that may induce more defects. A recent comparative study of shock-compressed materials suggested that Al$_2$O$_3$ with an unusually small S might collapse into a more incompressible phase above 340 GPa (38). The U$_2$S$_3$-type phase is denser than the CaIrO$_3$-type phase by ≈1.6% at 400 GPa and 300 K. However, their bulk moduli are very similar: 1,558 GPa and 1,552 GPa in the CaIrO$_3$-type and the U$_2$S$_3$-type phases, respectively. This contrasts with the case of NaMgF$_3$. Through the post-PPV transition in NaMgF$_3$, charge densities between Na and F increase and bonding between MgF$_6$ layers by Na atoms is strengthened (22). As a consequence, the compressibility of the b axis, which is perpendicular to the Mg-F
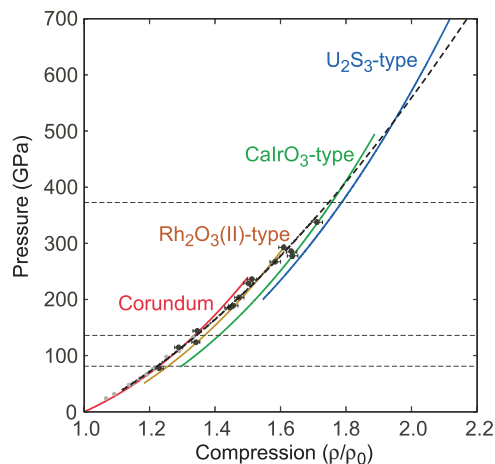
Fig. 6. Static LDA pressure vs. compression. ρ is the calculated density of each phase and ρ_0 is that of corundum at 0 GPa. Horizontal dashed lines represent calculated transition pressures. Numerical data of static LDA volumes for all four phases as functions of pressure, which are used to calculate compression, are given in supporting information (SI) Table S1. Experimental shock data are shown by black (34) and gray (35) circles. The black dashed line is a compression curve obtained by applying the Rankine–Hugoniot equations ($\rho = \rho_0 U_s / (U_s - U_p)$, $P = \rho_0 U_p U_s$) to a single linear fit to the Hugoniot data ($U_s = 8.74 + 0.957 U_p$) (35). Error bars for compression are estimated from the size of datum symbols in ref. 34, which correspond to an error of $\approx$1% in density. Estimated error bars for pressure are within datum symbols.

layers, decreases and the bulk modulus increases from 282 to 292 GPa at 50 GPa. In contrast, in Al_2O_3, the charge density between Al_1 and O atoms is already high in the $CaIrO_3$-type phase. There is no significant increase/decrease of charge density between the Al_2–O layers through the transition (Fig. 7), although the distance between layers decreases.

This post-PPV transition in Al_2O_3 occurs at pressures exceeding those achieved in the Earth's mantle ($\approx$135 GPa at the core–mantle boundary) and should not alter our views of this region. However, it might affect our understanding of the rocky mantles of recently discovered terrestrial exoplanets (39–41) because it could change the solubility of Al_2O_3 in $CaIrO_3$-type $MgSiO_3$. The change in coordination from 6 to 7 in the B site suggests that Al_2O_3 might ex-solve from $MgSiO_3$,
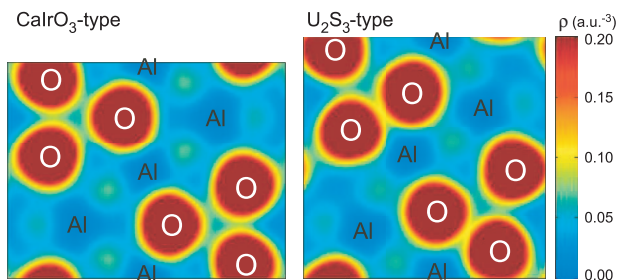
in particular, from the smaller 6-fold B site occupied by silicon in the $CaIrO_3$-type structure. The ex-solution of Al_2O_3 could affect the electrical and thermal conductivities of the $CaIrO_3$-type solid solution, as the incorporation of Al_2O_3 affects the electrical conductivity of $MgSiO_3$ perovskite in the presence of iron (4).

The prediction of the U_2S_3-type structure of Al_2O_3 suggests a likely close relationship between the multi-megabar crystal chemistry of planet-forming minerals and that of rare-earth sulfides, $RR'S_3$ (R, R' = lanthanoid or actinoid). Several crystal structures, including the corundum, $CaIrO_3$-type, and U_2S_3-type structures, are produced in the $RR'S_3$ family of compounds depending on atomic species and preparation conditions (42). In refs. 42 and 43, the structure corresponding to $CaIrO_3$-type is referred to as $NdYbS_3$-type.[†] The perovskite structure ($GdFeO_3$-type) also occurs in $RR'S_3$ compounds. At high temperature, $LaYbS_3$ is in the α phase with the $GdFeO_3$-type structure, whereas at low temperatures it adopts the β phase with the $NdYbS_3$-type (i.e., $CaIrO_3$-type) structure (44, 45). This is reminiscent of the postperovskite transition in $MgSiO_3$ with a positive Clapeyron slope (46–48). The relationship between these crystal structures and cation radii can be summarized as follows: the corundum structure occurs with small R and R' radii (e.g., Yb_2S_3), the U_2S_3-type structure with large radii, and the $CaIrO_3$-type and the $GdFeO_3$-type structures with large R in the A site and small R' in the B site (e.g., $NdYbS_3$ and α-$LaYbS_3$). This chemical-pressure effect produces a sequence of structures consistent with that induced by pressure in Al_2O_3. The ratios $(V_{Al_1} + V_{Al_2})/V_{Al_2O_3}$, where V_{Al_1} and V_{Al_2} are polyhedral volumes around Al_1 in the A site and Al_2 in the B site and $V_{Al_2O_3}$ is the formula unit volume, are 0.43, 0.62, and 0.68 in corundum, $CaIrO_3$-type, and U_2S_3-type Al_2O_3. These are very close to corresponding ratios in Yb_2S_3 (0.42) (49), $NdYbS_3$ (0.62) (43), and U_2S_3 (0.69) (50), respectively. In calculating V_{Al_1} and V_{Al_2}, the coordination numbers of Al_1 at the A site and Al_2 at the B site are set to be 6 and 6, 8 and 6, and 8 and 7 for corundum (where there is no distinction between Al_1 and Al_2), $CaIrO_3$-type, and U_2S_3-type Al_2O_3. Therefore, one can anticipate that other $RR'S_3$ structures may also play an important role in stabilizing sequioxides analogous to Al_2O_3 under pressure, or solid solutions and intermediate compounds of Fe_2O_3, Al_2O_3, CaO, MgO, FeO, and SiO_2 at multi-megabar pressures. This could have unexpected consequences for the internal structure and dynamics of exoplanets. In fact, Al_2O_3 in the α-Gd_2S_3-type structure, one of the major structures of $RR'S_3$ compounds, and the U_2S_3-type polymorph have very similar enthalpies (see Fig. 2).

[†]The $NdYbS_3$-type structure was first reported to have the $B22_12$ symmetry which is a subgroup of the $Cmcm$ group of the $CaIrO_3$-type structure (42, 43). However the $NdYbS_3$-type structure refined in the $B22_12$ symmetry is nearly indistinguishable from the $CaIrO_3$-type structure. The difference between them is very tiny; in the $B22_12$ $NdYbS_3$-type structure, the cation at the B site and one kind of sulfur are just slightly shifted from the $4a$ and $8f$ Wyckoff positions in the $Cmcm$ $CaIrO_3$-type structure. A recent x-ray diffraction study suggested the $NdYbS_3$-type structure should have the $Cmcm$ symmetry and be the same as the $CaIrO_3$-type structure (44).

Fig. 7. Charge densities on the (200) planes of $CaIrO_3$-type and U_2S_3-type Al_2O_3 at 400 GPa.

1. McQueen RG, Isaak DG (1990) Characterizing windows for shock-wave radiation studies. *J Geophys Res* 95(B13):21753–21765.
2. Chen NH, Silvera IF (1996) Excitation of ruby fluorescence at multimegabar pressure. *Rev Sci Instrum* 67:4275–4278 and references therein.
3. Wood BJ, Rubie DC (1998) The effect of alumina on phase transformations at the 660-kilometer discontinuity from Fe-Mg partitioning experiments. *Science* 273:1522–1524.
4. Xu Y, McCammon C, Poe BT (1998) The effect of alumina on the electrical conductivity of silicate perovskite. *Science* 282:922–924.
5. Zhang J, Weidner DJ (1999) Thermal equation of state of aluminum-enriched silicate perovskite. *Science* 284:782–784.
6. Frost DJ, *et al.* (2004) Experimental evidence for the existence of iron-rich metal in the Earth's lower mantle. *Nature* 428:409–412.
7. Li J, *et al.* (2004) Electronic spin state of iron in lower mantle perovskite. *Proc Natl Acad Sci USA* 101:14027–14030.
8. Tateno S, Hirose K, Sata N, Ohishi Y (2005) Phase relations in $Mg_3Al_2Si_3O_{12}$ to 180 GPa: Effect of Al on post-perovskite phase transition. *Geophys Res Lett* 32:L15306.
9. Nishio-Hamane D, Fujino K, Seto Y, Nagai T (2007) Effect of the incorporation of $FeAlO_3$ into $MgSiO_3$ perovskite on the post-perovskite transition. *Geophys Res Lett* 34:L12307.

GEOPHYSICS

10. Cynn H, Isaak DG, Cohen RE, Nicol MF, Anderson OL (1990) A high-pressure phase transition of corundum predicted by the potential induced breathing model. *Am Miner* 75:439–442.
11. Marton FC, Cohen RE (1994) Prediction of a high-pressure phase transition in Al_2O_3. *Am Mineral* 79:789–792.
12. Thomson KT, Wentzcovitch RM, Bukowinski MST (1996) Polymorphs of alumina predicted by first principles: Putting pressure on the ruby pressure scale. *Science* 274:1880–1882.
13. Funamori N, Jeanloz R (1997) High-pressure transformation of Al_2O_3. *Science* 278:1109–1111.
14. Mashimo T, *et al.* (2000) High-pressure phase transformation of corundum (α-Al_2O_3) observed under shock compression, *Geophys Res Lett* 27:2021–2024.
15. Lin JF, *et al.* (2004) Crystal structure of a high-pressure/high-temperature phase of alumina by in situ X-ray diffraction. *Nat Mater* 3:390–393.
16. Caracas R, Cohen RE (2005) Prediction of a new phase transition in Al_2O_3 at high pressures. *Geophys Res Lett* 32:L06303.
17. Oganov AR, Ono S (2005) The high-pressure phase of alumina and implications for Earth's D'' layer. *Proc Natl Acad Sci USA* 102:10828–10831.
18. Tsuchiya J, Tsuchiya T, Wentzcovitch RM (2005) Transition from the Rh_2O_3(II)-to-$CaIrO_3$ structure and the high-pressure-temperature phase diagram of alumina. *Phys Rev B* 72:020103(R).
19. Ono S, Oganov AR, Koyama T, Shimizu H (2006) Stability and compressibility of the high-pressure phases of Al_2O_3 up to 200 GPa: Implications for the electrical conductivity of the base of the lower mantle. *Earth Planet Sci Lett* 246:326–335.
20. Umemoto K, Wentzcovitch RM, Allen PB (2006) Dissociation of $MgSiO_3$ in the cores of gas giants and terrestrial exoplanets. *Science* 311:983–986.
21. Umemoto K, Wentzcovitch RM, Weidner DJ, Parise JB (2006) $NaMgF_3$: A low-pressure analog of $MgSiO_3$. *Geophys Res Lett* 33:L15304.
22. Umemoto K, Wentzcovitch RM (2006) Potential ultrahigh pressure polymorphs of ABX_3-type compounds. *Phys Rev B* 74:224105.
23. Perdew JP, Zunger A (1981) Self-interaction correction to density-functional approximations for many-electron systems. *Phys Rev B* 23:5048–5079.
24. Perdew JP, Burke K, Ernzerhof M (1996) Generalized gradient approximation made simple. *Phys Rev Lett* 77:3865–3868.
25. Vanderbilt D (1990) Soft self-consistent pseudopotentials in a generalized eigenvalue formalism. *Phys. Rev. B* 41:7892–7895(R).
26. Wentzcovitch RM (1991) Invariant molecular-dynamics approach to structural phase transitions. *Phys Rev B* 44:2358–2361.
27. Wentzcovitch RM, Martins JL, Price GD (1993) Ab initio molecular dynamics with variable cell shape: Application to $MgSiO_3$. *Phys Rev Lett* 70:3947–3950.
28. Giannozzi P, de Gironcoli S, Pavone P, Baroni S (1991) Ab initio calculation of phonon dispersions in semiconductors. *Phys Rev B* 43:7231–7242.
29. Baroni S, de Gironcoli S, Dal Corso A, Giannozzi P (2001) Phonons and related crystal properties from density-functional perturbation theory. *Rev Mod Phys* 73:515–562.
30. Wallace D (1972) *Thermodynamics of Crystals* (Wiley, New York), Chap. 4.
31. Baroni S, *et al*. (2006) Quantum-ESPRESSO. Available at http://www.pwscf.org/. Accessed August 13, 2006.
32. Hyde BG, Andersson S, Bakker M, Plug CM, O'Keeffe M (1979) The (twin) composition plane as an extended defect and structure-building entity in crystals. *Prog Solid State Chem* 12:273–327.
33. d'Amour H, Schiferl D, Denner W, Schulz H, Holzapfel WB (1978) High-pressure single-crystal structure determinations for ruby up to 90 kbar using an automatic diffractometer. *J Appl Phys* 48:4411–4416.
34. Erskine D (1994) High pressure Hugoniot of sapphire. *High Pressure Science and Technology–1993*, eds Schmidt SC, Shaner JW, Samara GA, Ross M (AIP Press, New York).
35. Marsh S, *et al*. (1980) LASL Shock Hugoniot Data (Univ of California Press, Berkeley), p 260.
36. Urtiew PA (1974) Effect of shock loading on transparency of sapphire crystals. *J Appl Phys* 45:3490–3493.
37. Weir ST, Michell AC, Nellis WJ (1996) Electrical resistivity of single-crystal Al_2O_3 shock-compressed in the pressure range 91–220 GPa (0.91–2.20 Mbar). *J Appl Phys* 80:1522–1525.
38. Mashimo T, *et al*. (2006) Transition to a virtually incompressible oxide phase at a shock pressure of 120 GPa (1.2 Mbar): $Gd_3Ga_5O_{12}$. *Phys Rev Lett* 96:105504.
39. Guillot T (2004) Probing the giant planets. *Phys Today* 57:63–69.
40. Rivera EJ, *et al*. (2005) A ~7.5 $M_\oplus$ planet orbiting the nearby star, GJ 876. *Astrophys J* 634:625–640.
41. Valencia D, O'Connell RJ, Sasselov D (2006) Internal structure of massive terrestrial planets. *Icarus* 181:545–554.
42. Flahaut J (1979) Sulfides, selenides, and tellurides. *Handbook on the Physics and Chemistry of Rare-Earths*, eds Gschneidner KA, Jr, Eyring LR (North-Holland, Amsterdam), Vol 4, p 1 and references therein.
43. Carré PD, Laruelle P (1974) Crystal structure of neodymium ytterbium sulphide, $NdYbS_3$ (Translated from French). *Acta Crystallogr B* 30:952–954.
44. Mitchell K, Somers RC, Huang FQ, Ibers JA (2004) Syntheses, structure, and magnetic properties of several $LnYbQ_3$ chalcogenides, Q=S, Se. *J Solid State Chem* 177:709–713.
45. Rodier PN, Julien R, Tien V (1983) Polymorphism of $LaYbS_3$—Refinement of the structure of 2 varieties (Translated from French). *Acta Crystallogr C* 39:670–673.
46. Murakami M, Hirose K, Kawamura K, Sata N, Ohishi Y (2004) Post-perovskite phase transition in $MgSiO_3$. *Science* 304:855–858.
47. Tsuchiya T, Tsuchiya J, Umemoto K, Wentzcovitch RM (2004) Phase transition in $MgSiO_3$ perovskite in the earth's lowe mantle. *Earth Planet Sci Lett* 224:241–248.
48. Oganov AR, Ono S (2004) Theoretical and experimental evidence for a post-perovskite phase of $MgSiO_3$ in Earth's D'' layer. *Nature* 430:445–448.
49. El Fadli Z, Lemoine P, Guittard M, Tomas A (1994) Structure of ytterbium sulfide, YbS_2S_3 (Translated from French), (1983) *Acta Crystallogr C* 50:166–168.
50. Wyckoff RWG (1963) *Crystal Structures* (Interscience Publishers, New York), Vol 2.